

Temperature Estimation for a Plasma-Propelled Rocket Engine Inferential Measurement Using Optical Emission Spectroscopy Data

SHANE A. LYNN, JOHN V. RINGWOOD, and JUAN IGNACIO DEL VALLE GAMBOA

The vast majority of rocket engines rely exclusively on chemical combustion to achieve thrust in the vacuum of space. However, a new generation of electrically mediated propulsion systems for spacecraft produce thrust from a fuel propellant using electric energy. For example, in ion thrusters, neutral gas is first ionized, and the ions are accelerated using either the Coulomb force or the Lorentz force, based on electric or magnetic fields, respectively. The acceleration of ions away from the spacecraft propels the craft in the opposite direction by Newton's third law of motion.

The variable specific impulse magnetoplasma rocket (VASIMR) is an electric propulsion technology being developed by the Ad Astra Rocket Company at its facilities in Houston, Texas, USA, and in Liberia, Costa Rica. To produce thrust, the VASIMR engine uses a highly ionized plasma (see "What Is a Plasma?") accelerated with magnetic fields to produce thrust. In VASIMR, plasma is generated with a helicon antenna using radio frequency waveforms at the frequency 13.56 MHz. Helicon discharges are known to be efficient methods for plasma production [1]. Initially, electromagnetic waves from the antenna energize free electrons present in a neutral gas fuel. These electrons then ionize atoms in the gas through energetic collisions to create a plasma. Charged particles in the plasma follow helical paths along magnetic field lines due to the Lorentz force, which is proportional to the charge on the particle, the velocity of the particle, and the strength of the magnetic field. Carefully designed electromagnets form magnetic field patterns that confine the plasma and move it from the helicon to the ion cyclotron resonant heating (ICRH) section of the rocket. In the ICRH section, a second helicon antenna excites the ions at precisely their gyrofrequency, further energizing the propellant gas [2]. The gyrofrequency of a charged particle is the frequency of rotation of the particle as it spirals in a magnetic field. This frequency is directly proportional to the charge of the particle and the magnetic field strength and inversely proportional to the mass of the particle. In the last portion of the rocket, a final group of magnets, comprising the magnetic nozzle, accelerate the plasma away from the craft along expanding magnetic field lines. The energized plasma physically detaches from the engine and its

magnetic field, thus creating thrust. The exhaust velocities from VASIMR are expected to reach as high as 120 km/s [3] in final prototypes. For near-term applications of VASIMR, large solar arrays are expected to generate electric power for the rocket [4]. The VASIMR engine is depicted in Figure 1.

Compared to alternative electric propulsion technologies, VASIMR has many advantages as a potential space propulsion system. Plasma is produced inductively in the engine, negating the requirement for electrodes to be in contact with the plasma. This electrodeless design allows greater power densities to be reached for longer periods of time than conventional magnetoplasma or ion engines, without fear of electrodes becoming damaged or wearing out. This design is essential for missions requiring months or years of continuous rocket operation. The propellant gas, which is argon, is inexpensive, chemically inert, and widely available.

The greatest advantage of VASIMR is that it produces thrust very efficiently compared to chemical rockets. The efficiency of a jet or rocket engine is measured by the momentum change per unit weight of consumed propellant. This characteristic, which is measured in seconds, is termed the *specific impulse* of the engine. Used as a measure of economy between rocket engines, specific impulse is comparable to

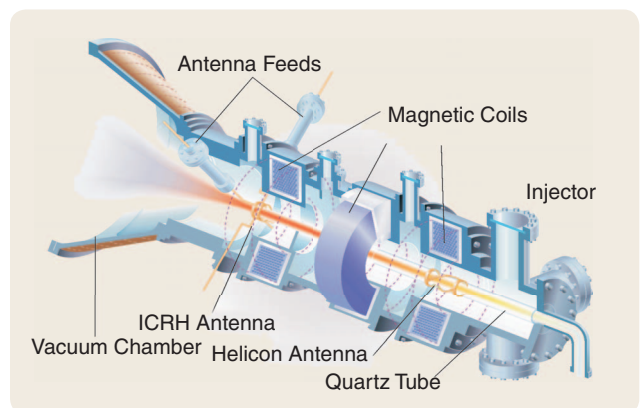


FIGURE 1 Schematic of the variable specific impulse magnetoplasma rocket (VASIMR) engine. The VASIMR consists of three main sections, namely, a helicon plasma source, an ion cyclotron resonance heating (ICRH) plasma accelerator, and a magnetic nozzle that accelerates the plasma away from the craft to produce final thrust [2]. For prototypes on Earth, a 5-m³ vacuum chamber is used to simulate the vacuum of outer space. Image courtesy of NASA.

What Is a Plasma?

First identified by Sir William Crookes in 1879, plasma, often referred to as the fourth state of matter, is essentially a super-heated gas. Plasma is the most abundant state of matter in the universe. The aurora borealis, the sun's corona, the tails of comets, and the solar wind are all examples of plasmas that exist in space.

At high temperatures, the atoms and molecules of a gaseous substance become ionized as a result of the high levels of energy that the particles obtain. The process of ionization of atoms is the removal of one or more electrons from their outer shells. Plasmas are often characterized by their degree of ionization, which can vary depending on the application in question. Many plasmas used in plasma processing may have a 1–10% degree of ionization whereas plasma used in nuclear fusion may become fully ionized. With sufficient power, plasma in the VASIMR engine approaches 100% ionization. Since only the ionized particles can be accelerated magnetically to produce thrust, a high ionization percentage is desirable. Increasing the efficiency of the ionization process is a key challenge to the VASIMR project.

Hence plasma is made up of ions, electrons, and neutral atoms that move as interpenetrating liquids, constantly interacting and colliding with each other. Overall, the plasma is electrically neutral. Plasmas luminesce due to the constant excitation and relaxation processes that occur within their molecules (see “What Is Optical Emission Spectroscopy?”) with a

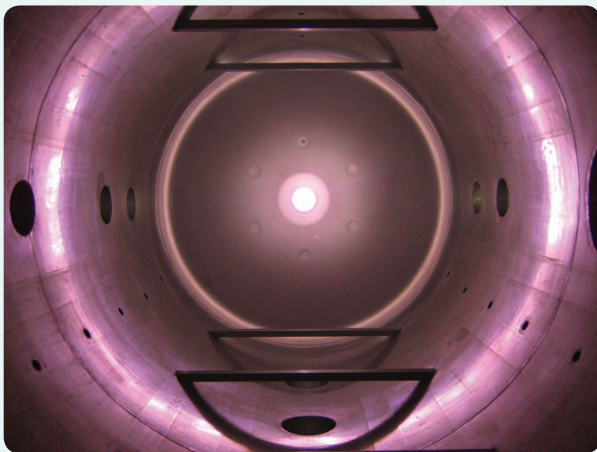


FIGURE S1 View of helicon source from rear of vacuum chamber. The purple hue of the plasma is a result of the photons released from the excitation and relaxation of argon ions.

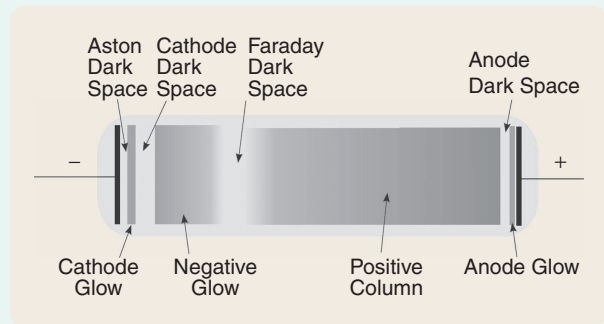


FIGURE S2 DC plasma discharge. A dc plasma is formed by generating a dc voltage between two electrodes in a neutral gas at low pressure. Electrons move in response to the resulting electric field to create ions and form the labeled discharge regions. For a full description of these regions see [S1].

color that is characteristic of its constituent gases and their level of excitation. The purple glow of VASIMR's argon discharge is shown in Figure S1.

Plasmas are generated by encouraging ionization of atoms in a neutral gas. Ionization can be achieved by forcing energetic collisions between particles, bombardment with ionizing radiation, or using strong electric fields on atom's valence electrons. In a capacitively coupled plasma, two electrodes are placed close together and one is driven with an electric voltage. Free electrons move in response to the resulting electric field and cause ionization through collisions with neutral particles. These new collisions free more electrons, leading to an avalanche effect. A plasma quickly forms between the electrodes. These sources generate *capacitively coupled* discharges, since power is capacitively transferred to the neutral gas. Power can also be coupled inductively, leading to an inductively coupled plasma. The supplied voltage can be either dc or ac to create a plasma. DC discharges are simpler and have a definite structure as shown in Figure S2.

The charged particles in plasmas are manipulated in many applications for a variety of purposes including semiconductor processing, display technology, plasma spraying, power systems, and waste disposal [S2].

REFERENCES

- [S1] B. Chapman, *Glow Discharge Processes*. New York: Wiley, 1980.
- [S2] P. McKenna, “Could your trashcan solve the energy crisis?” *New Scientist*, vol. 202, no. 2705, pp. 33–35, 2009.

a miles-per-gallon, or liters-per-100 km rating for a motor vehicle. Chemical rockets used in spacecraft typically produce thrusts of 60,000–70,000 N at a specific impulse of 300 s [5]. High thrusts from chemical rockets provide a large acceleration but with a quick consumption of fuel. VASIMR produces relatively low thrusts of 5–10 N, but, with a high specific impulse of between 5000–15,000 s [6] and the ability

to sustain thrust for prolonged periods, the relatively small acceleration ultimately achieves higher spacecraft velocities for a given fuel supply. As shown in Figure 2, over the vast distances involved in interplanetary travel, a VASIMR-equipped spacecraft can reach distant destinations in less time using the same quantity of fuel. VASIMR gets its name from its capability to vary its specific impulse performance in order to

produce more or less thrust. Extra thrust can be produced by the engine, but at the expense of a lower specific impulse.

Although significantly more than 10 N of thrust is required to produce a substantial fraction of the gravitational force felt on Earth, the constant acceleration from continuous VASIMR operation results in an artificial gravity effect on board spacecraft, reducing the physiological effects that weightless environments have on the human body.

Heat is an undesirable by-product of helicon plasma production. The helicon stage of VASIMR is comprised of a ceramic gas containment tube surrounded by a helicon antenna. Since the ionization mechanisms are not completely efficient, some neutral atoms do not acquire sufficient energy from collisions to expel electrons into the plasma. Although neutrals might achieve an excited state temporarily from such collisions, neutrals eventually return to their base configuration, releasing energy as photons in the visible and UV spectra. This energy radiates away and is absorbed by the gas tube and other nearby engine elements. In addition, high velocity neutrals can be created as a result of energetic collisions between particles. These newly formed neutral atoms are not affected by the magnetic field lines and continue on their original paths at high velocities, ultimately colliding with other particles or the gas containment tube. Furthermore, since the tube is not completely transparent to radio-frequency energy, it absorbs part of the energy transmitted by the antenna. All of these effects produce significant and rapid heating of the gas tube as shown in Figure 3.

Temperature control of the gas tube is critical to the VASIMR design since the quartz tube can reach absolute temperatures and achieve temperature gradients beyond its allowable limits. The VASIMR prototype uses superconducting magnets located close to the gas tube to produce magnetic fields. These magnets operate at cryogenic temperatures that must not be affected by the gas tube temperature. Although laboratory prototypes of the rocket use thermocouples to monitor heating of the gas containment tube, these sensors cannot be used in the final flight design because they would obstruct cooling designs that are in development. Thermocouple temperature signals are also subject to electromagnetic interference from the helicon antenna and, furthermore, the thermocouples themselves are physically fragile.

The goal of this work is to develop a prediction system for estimating

the temperature distribution on the gas containment tube in the helicon section of VASIMR, in the absence of direct temperature measurements using thermocouples. In particular, we use a state-space prediction model along with optical emission spectroscopy (OES) (see "What Is Optical Emission Spectroscopy?") measurements from the plasma for temperature-estimate correction. Since OES readings directly correlate to the excitation of non-ionized neutrals in the plasma, and since these neutrals contribute to the heating of the gas containment tube, we believe that OES can be used to assist in temperature estimation.

This article demonstrates a temperature-estimation strategy for a plasma-rocket engine. In particular, we estimate spatially distributed temperatures from OES measurements. The estimator model is built using a state-space realization for which direct-state measurements are used to identify the state-space model parameters. However, such direct state measurements are not available in the operational system, requiring the development of a state estimator. Experimental results demonstrate the effectiveness of the scheme.

HELICON SYSTEM

In the VASIMR engine, high-density plasma is produced using a helicon wave source. The helicon section of the engine, which is depicted in Figure 4, consists of a helicon

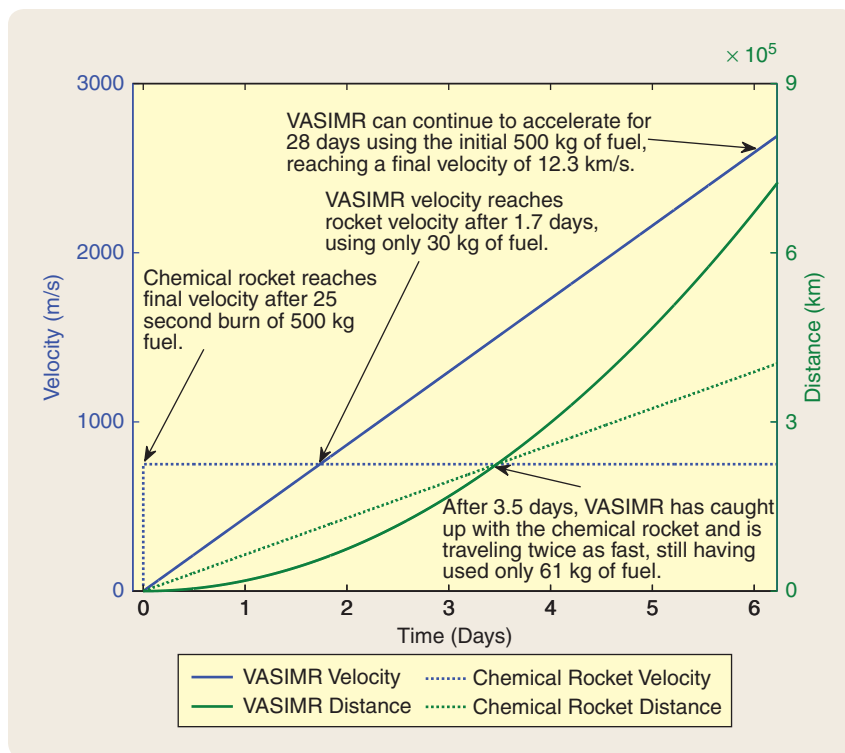


FIGURE 2 Example performance of a variable specific impulse magnetoplasma rocket (VASIMR) propelled spacecraft compared to a chemical rocket propelled spacecraft. This figure compares the velocity and distance profiles for a hypothetical 2000 kg mass accelerated using a thrust of 60,000 N from a chemical rocket with specific impulse of 300 s and a thrust of 10 N from VASIMR with a specific impulse of 5000 s. Both spacecraft start with zero initial velocity and 500 kg of fuel.

What Is Optical Emission Spectroscopy?

Optical emission spectroscopy (OES) measures light emitted from a plasma as a function of wavelength, time, and location and is one of the most commonly used plasma diagnostic probes [7].

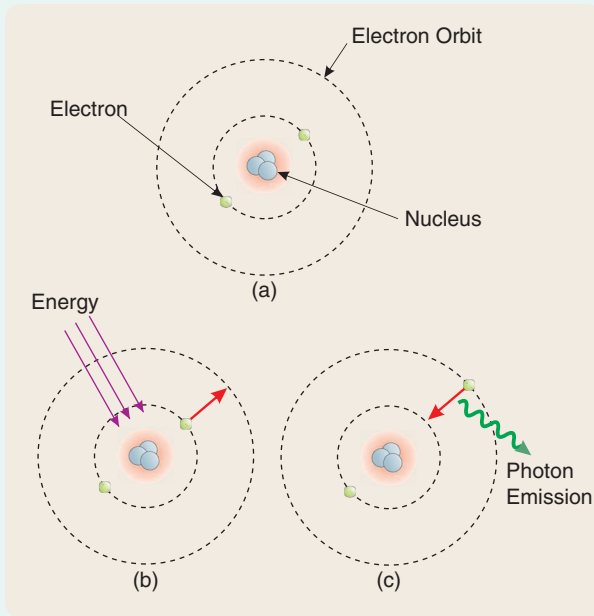


FIGURE S3 Photon emission from an atom. (a) Atom in neutral state. All electrons are in the lowest orbits available. (b) The excitation process. Energy is introduced to the atom from an outside source to excite electrons to higher energy orbits. (c) Relaxation. Excited electrons fall from their unstable outer orbits and release energy in the form of photons in the process.

In a plasma, particles are continuously undergoing the processes of excitation from the sustaining external energy source and relaxation, which is the loss of the previously gained energy. According to the Bohr model of atomic structures [S3], electrons orbit the nucleus of an atom in fixed quantized energy levels. When an atom gains energy, electrons move farther away from the nucleus to higher energy levels. In a random fashion, electrons eventually fall from this unstable position to a de-energized state, releasing the previously gained energy in the form of a photon of light. The wavelength of the released photon is inversely proportional to the energy gap between the two energy levels that have been crossed. The energy of the photon is given by

$$E = \frac{hc}{\lambda}, \quad (\text{S1})$$

where h is Planck's constant, c is the speed of light in a vacuum, and λ is the wavelength of the photon. The excitation and relaxation processes are depicted in Figure S3.

Since each species has an individual electron configuration, and as energy levels are quantized allowing only certain transitions, the luminescence from plasma is a characteristic of its gaseous composition and the excitation level of its molecules.

In an optical emission spectrometer, light received from a luminescent source is first dispersed into its constituent wavelengths using a diffraction grating, prism, or set of filters. The dispersed light is then focused on a photodetector that records the intensity of each individual wavelength in every sample. Various photodetector technologies are available, including photomultiplier tubes, photodiodes, and charged coupled devices [7].

antenna wrapped around a quartz tube through which neutral gas is flowing. Electromagnetic coils, which maintain a magnetic field parallel to the gas flow, surround the quartz tube. Helicon discharges are a form of inductively coupled plasmas where a magnetic field is used to assist in the production of high-density plasma. The magnetic field has three main functions. First, it increases how far an electromagnetic wave penetrates into the plasma, also known as the *skin depth*. With the magnetic field in place in a helicon discharge, the electromagnetic waves can penetrate into the entire plasma. Second, the magnetic field helps to confine the electrons in the plasma for an extended time. Finally, the magnetic field gives the operator the ability to vary plasma parameters such as the plasma density uniformity [7]. The magnetic field confines the plasma to the center of the quartz tube and guides the plasma flow to the next section of the engine.

A helicon wave is defined as a right-handed polarized wave that propagates in a radially confined magnetized plasma for frequencies $\omega_{ci} \ll \omega \ll \omega_{ce}$, where ω_{ci} is the ion gyrofrequency, ω is the frequency of the helicon wave, and

ω_{ce} is the electron gyrofrequency [8]. A detailed review of the discovery and advances in helicon research is provided in [8] and [9].

When helicon input conditions such as pressure, power, and magnetic field strength are varied over a broad range, helicon discharges are seen to have several distinct modes of operation, separated by discontinuous jumps [10]. Capacitive, inductive, and helicon-wave modes can occur [11]. Jumps between modes, which are accompanied by dramatic changes in plasma density (by factors of two or three), can arise during smooth variations in input variables. The experiments described in this work have power settings of 0.8–1.4 kW, where the system operates in an inductive mode. Within each operational mode, the use of a linear estimator model is justified, while multiple linear models could be employed to cover a range of modes.

For the purposes of this article, the helicon plasma source is visualized as a standalone system. The flow of argon gas into the quartz tube, the dc current in the electromagnets, and the power delivered to the helicon antenna can all be varied independently. Changes in these

The duration of time for which photons of light are accumulated in the photodetector is the *integration time*. The integration time effectively serves as a lowpass filter for the light intensity signals, where a longer integration time corresponds to a lower bandwidth, while also affecting the signal-to-noise (S/N) ratio of the measured light intensity. Since the noise level is constant, increases in integration time produce a roughly proportional increase in S/N ratio. The choice of integration time is therefore a tradeoff between S/N and bandwidth of the OES signals. Since a single integration time for the photodetector must be specified and mean intensities of the spectral lines vary with wavelength, care must be taken to ensure that weaker spectral lines appear above the noise threshold, while stronger lines do not saturate the photodetector. Figure S4 shows the OES spectrum from the VASIMR engine. Note that a large number of spectral lines arise from the argon discharge, each one corresponding to an energy level transition in the excited argon atoms.

Absolute concentrations of constituent gases of a plasma are difficult to obtain from OES measurements as spectral line intensities can only be compared relative to each other. Absolute concentrations are sometimes obtained using *actinometry* [S4]. In actinometry, a measured amount of an inert gas is added to the discharge, and intensities of known OES lines are compared to those present in the plasma, allowing absolute concentrations to be calculated.

OES is nonintrusive, inexpensive, and simple to install on systems where visual access to the plasma is available. OES is commonly used in semiconductor processing to monitor the status of plasma-based processes such as semiconductor etch [S5].

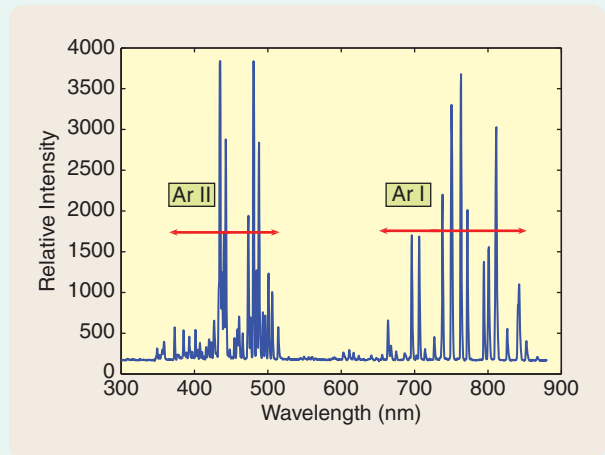


FIGURE S4 Argon spectrum from the variable specific impulse magnetoplasma rocket. Two distinct groups of emission lines can be seen on the plot. Ar I denotes the first ionization level of an argon atom. Ar II has higher energy, and hence a lower emission wavelength, as shown in the figure.

REFERENCES

- [S3] N. Bohr, “On the constitution of atoms and molecules part I,” *Philos. Mag.*, vol. 26, no. 151, pp. 1–26, 1913.
- [S4] J. W. Coburn and M. Chen, “Optical emission spectroscopy of reactive plasmas: A method for correlating emission intensities to reactive particle density,” *J. Appl. Phys.*, vol. 51, pp. 3134–3136, 1980.
- [S5] S. J. Hong, G. S. May, and D. C. Park, “Neural network modeling of reactive ion etching using optical emission spectroscopy data,” *IEEE Trans. Semicond. Manufact.*, vol. 16, no. 4, pp. 598–608, 2003.

input variables result in variations in the plasma generated, with consequent variations in the optical emission from the plasma and heat distribution on the surface of the quartz tube.

OPTICAL DATA PREPROCESSING

OES data are collected from the plasma downstream from the helicon section, as depicted in Figure 4. Several steps are undertaken to extract the features of interest, and to restructure the optical data into a form that is useful for estimation.

An Ocean Optics S2000 spectrometer, sampled once per second, is used to collect the OES data. At each sampling instant, the intensity of the plasma optical emission is recorded at 2047 wavelengths between 200–850 nm with an integration time of 200 ms. Analysis of the spectral intensity lines reveals that many lines are highly correlated in time, with correlation coefficients greater than 0.75. Due to the high levels of correlation between the time series of intensity measurements at each wavelength, principal component analysis (PCA) is used to identify the main uncor-

related, or independent, components that contribute to the variance in these time series.

Before PCA is performed on the set of data $X \in \mathbb{R}^{a \times b}$, made up of a samples (rows) of b variables (columns), we offset each variable to have zero mean. Typically, normalization to unit variance is also performed when the original data has multiple scales to give all variables equal initial importance for the analysis. However, unit variance normalization is not needed in our studies since all OES wavelengths are recorded on the same intensity scale. The VASIMR data matrix X is made up of 2047 wavelengths that correspond to the columns of X , sampled 15,000 times. Hence, for the PCA calculations, X has dimensions $15,000 \times 2047$. PCA performs an eigenvalue decomposition of the covariance matrix of X , which decomposes X as the sum of the outer product of the column vectors t_i and p_i plus a residual matrix E [12]. We thus have

$$X = t_1 p_1^T + t_2 p_2^T + \cdots + t_i p_i^T + E \quad (1)$$

$$= TP^T + E, \quad (2)$$

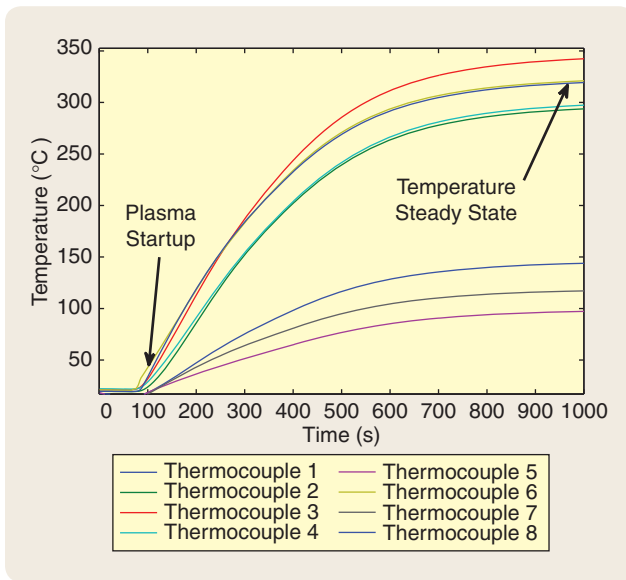


FIGURE 3 Gas tube temperatures during plasma startup. Temperatures rise quickly after a stable plasma is established. Note the large variability in temperatures around the tube in steady state. The nonuniform distribution occurs since the heat deposited by the plasma varies with position due to the mechanisms of energy transfer to the plasma by the helicon antenna.

where

$$T = [t_1 \ t_2 \ \dots \ t_l], P = [p_1 \ p_2 \ \dots \ p_l], \quad (3)$$

and l is the number of principal components. The vectors $t_i \in \mathbb{R}^{a \times 1}$ are the *scores* and $T \in \mathbb{R}^{a \times l}$ the score matrix; the vectors $p_i \in \mathbb{R}^{b \times 1}$ are the *loadings*, and $P \in \mathbb{R}^{b \times l}$ is the loadings matrix. For PCA, the decomposition of X is such that the columns of the loading matrix P are orthonormal to each other, and the columns of the score matrix T are orthogonal to each other. The first principal component is the linear combination of the m original variables that explains the greatest amount of variability ($t_1 = Xp_1$). For the VASIMR data, this first principal component is the variable created from a linear combination of recorded wavelength intensi-

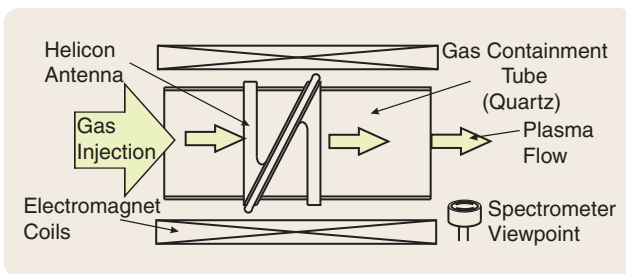


FIGURE 4 Helicon section of the variable specific impulse magnetoplasma rocket (VASIMR). A helicon discharge uses a right-hand circularly polarized wave to efficiently ionize a neutral gas to plasma state. The helicon is surrounded by electromagnetic coils that maintain a magnetic field along the axis of the antenna to assist in high-density plasma production.

ties that explains the greatest portion of the variance in the OES data. In the m -dimensional variable space, the loading vector p_1 defines the direction of the greatest variance in space spanned by the OES data matrix X [13]. The components are arranged in descending order, consistent with the amount of variance explained in the original data set by each component [14].

Overall, the loadings represent how the original wavelengths are combined to form the principal components, the scores are the principal component variables modeling the original OES data, and, finally, the residual E represents the data that is left unrepresented by the model. For a matrix X of rank r , r principal components can be calculated. However, the first k ($k < r$) of the principal components may be sufficient to explain the majority of the variance in the data. If $k = \dim(X)$, then $E = 0$, and the representation of the data is exact using the principal components.

For the OES data recorded during the VASIMR experiments, it is found that just three principal components are capable of representing 97% of the original data variance. Reducing the OES data set from 2048 correlated variables to only three orthogonal principal components significantly reduces computational requirements during estimation and shows that the underlying process driving OES variation can be adequately described by three independent time series.

MODEL IDENTIFICATION

The VASIMR helicon section has three manipulated inputs, namely, the gas flow rate, the electromagnet current, and the radio-frequency antenna power. The outputs y of the system are the three principal components arising from the PCA analysis of the OES data. The states x of the system are temperatures at 18 locations on the gas containment tube, which are measured using thermocouples bonded to the outside surface of the tube. Fifteen thermocouples are arranged along three longitudinal lines of five thermocouples, at angular locations 0 , $2\pi/3$, and $4\pi/3$ rad, while three thermocouples are positioned at intermediate angles between the longitudinal lines. Figure 5 shows the layout of the thermocouple array on the gas containment tube. Figure 6 shows temperatures recorded from the thermocouples arranged in longitudinal lines. The hottest part of the gas tube is in the center, in the region surrounding the helicon antenna, corresponding to the area of plasma production. Thermocouples are sampled at 1 Hz using a National Instruments analog-to-digital convertor interfaced with a LabView control system for the VASIMR. A state-space model of the form

$$x_{k+1} = Ax_k + Bu_k, \quad (4)$$

$$y_k = Cx_k, \quad (5)$$

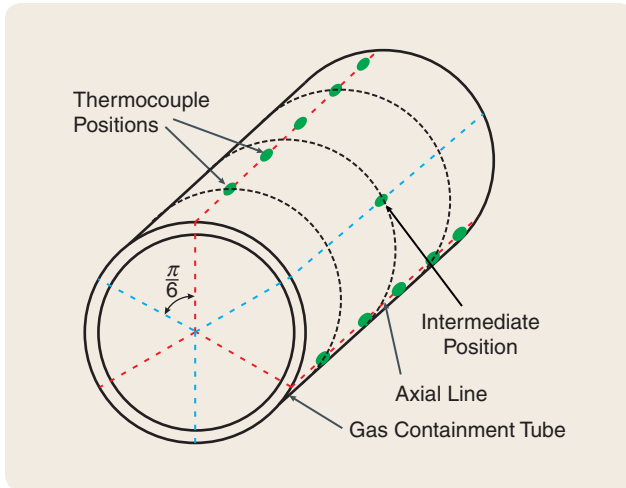


FIGURE 5 Thermocouple positions on the gas containment tube. An array of 18 thermocouples is used to record temperature information from the outside surface of the gas tube. The thermocouples are arranged in three longitudinal lines of five sensors, with three extra thermocouples placed in intermediate positions between these lines.

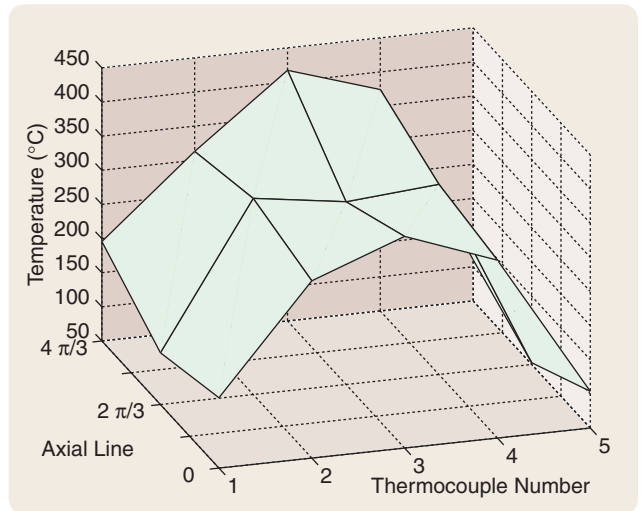


FIGURE 6 Sample temperature values recorded from thermocouple array. The region at the center of the tube, near thermocouple positions 2, 3, and 4, corresponds to the region inside the helicon antenna, where plasma is produced and, consequently, where the highest temperatures are recorded.

is used to model the system, where $x \in \mathbb{R}^{18}$ represents the measured temperatures, $u \in \mathbb{R}^3$ corresponds to the inputs to the helicon, and $y \in \mathbb{R}^3$ denotes the outputs of the system, that is, the first three principal components of the OES spectra. Hence, $A \in \mathbb{R}^{18 \times 18}$, $B \in \mathbb{R}^{18 \times 3}$, and $C \in \mathbb{R}^{3 \times 18}$.

For model identification, data records for u , y , and x are available for various system excitations. We determine the model parameters by first expanding (4) as

$$\begin{bmatrix} x_1(k+1) \\ x_2(k+1) \\ \vdots \\ x_n(k+1) \end{bmatrix} = \begin{bmatrix} a_{11} & a_{12} & \cdots & a_{1n} \\ a_{21} & a_{22} & \cdots & a_{2n} \\ \vdots & \vdots & \cdots & \vdots \\ a_{n1} & a_{n2} & \cdots & a_{nm} \end{bmatrix} \begin{bmatrix} x_1(k) \\ x_2(k) \\ \vdots \\ x_n(k) \end{bmatrix} + \begin{bmatrix} b_{11} & b_{12} & \cdots & b_{1m} \\ b_{21} & b_{22} & \cdots & b_{2m} \\ \vdots & \vdots & \cdots & \vdots \\ b_{n1} & b_{n2} & \cdots & b_{nm} \end{bmatrix} \begin{bmatrix} u_1(k) \\ u_2(k) \\ \vdots \\ u_m(k) \end{bmatrix}. \quad (6)$$

We can write out the first row of (6) for $k+1, k+2, \dots, k+N$ as shown in (7) at the bottom of the page. Equation (7) is of the form

$$\begin{bmatrix} x_1(k+1) \\ x_1(k+2) \\ \vdots \\ x_1(k+N) \end{bmatrix} = \begin{bmatrix} x_1(k) & \cdots & x_n(k) & \cdots & \cdots & u_1(k) & \cdots & u_m(k) \\ x_1(k+1) & \cdots & x_n(k+1) & \cdots & \cdots & u_1(k+1) & \cdots & u_m(k+1) \\ \vdots & \vdots & \vdots & \vdots & \cdots & \vdots & \vdots & \vdots \\ x_1(k+N-1) & \cdots & x_n(k+N-1) & \cdots & \cdots & u_1(k+N-1) & \cdots & u_m(k+N-1) \end{bmatrix} \begin{bmatrix} a_{11} \\ \vdots \\ a_{1n} \\ b_{11} \\ \vdots \\ b_{1m} \end{bmatrix}. \quad (7)$$

$$Y = \Phi\Theta, \quad (8)$$

which has the least squares solution [15]

$$\hat{\Theta} = (\Phi^T\Phi)^{-1}\Phi^TY. \quad (9)$$

A total of n least-squares problems are solved to obtain all rows of the estimates \hat{A} and \hat{B} of A and B . A similar formulation is used to estimate \hat{C} .

STATE ESTIMATION

Measurements of only u and y are available during normal VASIMR operation, where thermocouples are not available. We use these measurements to estimate the state vector x of gas tube temperatures. In both operational and experimental modes of VASIMR, the components of the input vector u , which are the gas flow rate, the electromagnetic current, and the radio-frequency antenna power, are predetermined before operation. With the model (4), (5), we can predict the state vector for a known input sequence u_{kr} assuming knowledge of the initial system state \hat{x}_0 . However, due to inaccuracies in both the model structure and parameters, and with significant uncertainty in the initial system states, state estimates from such a model are rarely

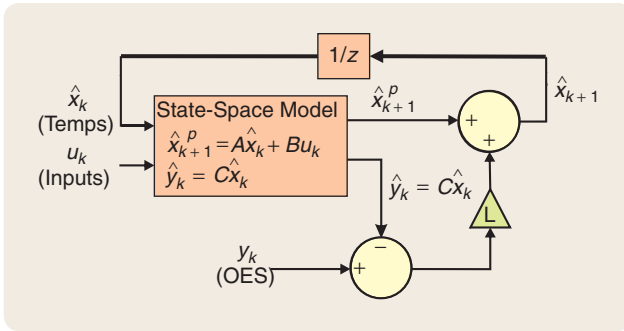


FIGURE 7 State-space model with estimation feedback. Errors between the estimated outputs and the measured outputs are used to update the estimated state vectors. In this diagram, \hat{x}^p denotes the state estimate before correction.

of practical value [16]. To decrease sensitivity to inaccurate or unknown initial conditions, a Luenberger observer is used to asymptotically estimate the state. The Luenberger observer [17] incorporates a correction term, based on the error between the modeled system output $C\hat{x}_k$ and the measured output y_k as

$$\hat{x}_{k+1} = \hat{A}\hat{x}_k + \hat{B}u_k + L(y_k - C\hat{x}_k), \quad (10)$$

where \hat{x}_k are the estimated states, and $L \in \mathbb{R}^{n \times m}$ is a gain matrix, adjusted to achieve satisfactory error dynamics. The estimator structure is shown in Figure 7, where \hat{x}^p is used to denote the state estimate before correction, that is,

$$\hat{x}^p = \hat{A}\hat{x}_k + \hat{B}u_k. \quad (11)$$

With the error defined as $e_k \equiv x_k - \hat{x}_{k_r}$, the error dynamics are found by subtracting the estimate of (10) from the state shown in (4) to give [16]

$$e_{k+1} = (\hat{A} - L\hat{C})e_k. \quad (12)$$

Assuming that the estimates \hat{A} , \hat{B} , and \hat{C} are sufficiently close to A , B , and C , a suitable matrix L can be determined using standard pole placement techniques, such as Ackermann's formula [16].

TABLE 1 Table of experiment input levels. Experimental levels for antenna power, magnet current, and gas flow are shown. The variations in experimental inputs are deliberately kept small to avoid helicon mode jumps. All combinations of the levels shown are explored, requiring 18 experiments in total. No mid value is used for the argon gas flow rate.

Value	Low	Mid	High
Antenna power (W)	800	1100	1400
Magnets (A)	800	1000	1200
Gas flow rate (sccm)	100	N/A	300

sccm: standard cubic centimeter per minute

EXPERIMENTATION

A series of 18 experiments are carried out to perform model identification. The experiments are designed such that the helicon remains in the same operational mode. Small perturbations in antenna power, gas flow, and magnet current are introduced as described in Table 1. Each experiment uses a different combination of input-variable values, and the resultant gas tube temperatures, monitored using the 18 thermocouples, are allowed to reach steady state where possible. Four of the experiments are repeated to ensure that consistent temperature and OES readings are recorded for repeated input conditions.

The transients in the OES principal components are found to be faster than those of the thermocouples. This difference in response time is attributed to the fact that the plasma reacts instantly to changes in the system inputs, while the gas tube temperatures reach steady state at a much slower pace. This discrepancy leads to difficulties in determining a satisfactory output matrix C for the model. To assist this effort, the dynamic response of the spectral data is slowed down using an exponentially weighted moving average filter. In this way, the output time constants are changed to have similar time constants to those of the states, allowing consistent estimation of a constant output matrix to be found. The filtered signal is denoted S_{k_r} and

$$S_{k+1} = \alpha S_k + (1 - \alpha)y_{k_r} \quad (13)$$

where y_k is the original OES principal component signal, and the filter coefficient α is set to 0.995. The effect of the filter on the OES principal components is depicted in Figure 8.

The experimental data set is used to create the state-space model, which is configured in closed-loop estimator form as shown in Figure 7. The estimator transient

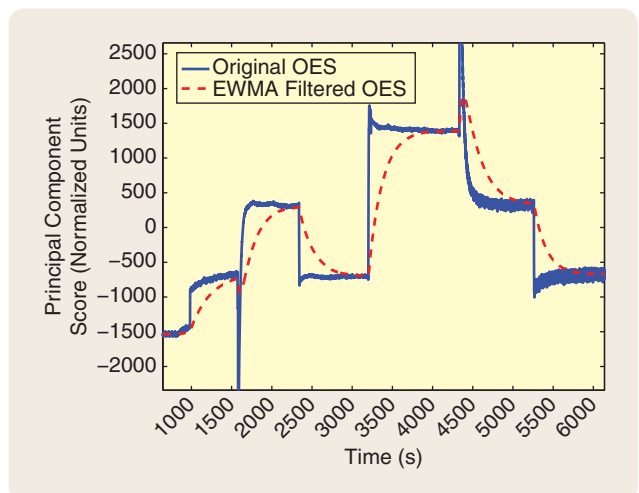


FIGURE 8 Application of exponentially weighted moving average filter on optical emission spectrometer (OES) data. The filter serves to slow the transients of the OES data, providing a linear relationship between OES and the temperature data.

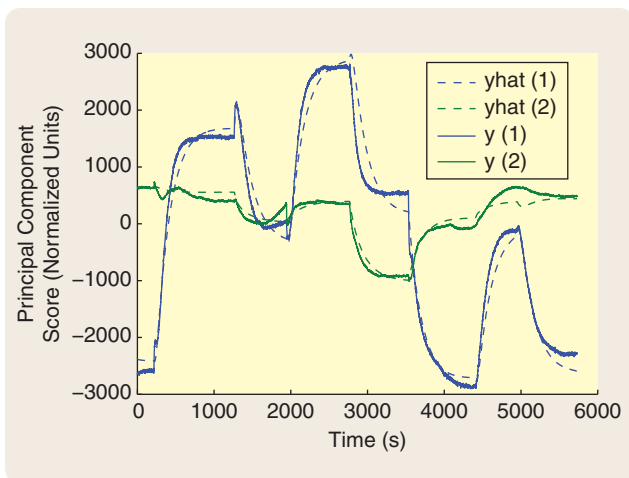


FIGURE 9 Comparison of model outputs in response to real state vectors with actual system outputs. The system outputs are defined to be the principal components of the optical emission spectroscopy data. It can be seen that the model output equation $y_k = Cx_k$ emulates the optical emission principal component scores when driven by the real system states.

response is set to be slightly faster than the transients found in the model state matrix A .

PERFORMANCE AND RESULTS

Output Model Validation

To validate the model derived, the output equation (5) of the state-space model is driven with the recorded temperature data x_k . Figure 9 compares the predicted principal components produced by the model to the real principal components of the OES data recorded. Two of the three OES principal components are shown in this diagram. The relationship between the states and the components is adequately represented by the linear relationship $y_k = Cx_k$, given the quality of the model/data match. The agreement between the model output and the real data confirms the existence of a linear relationship between the gas tube temperatures and the OES principal components.

Multistep Prediction Performance

As a further test of state-space model performance, the model is configured in an open-loop manner. In this configuration, no feedback term is included to correct the state and output estimations, corresponding to $L = 0$ in (10). We can see that the state estimate \hat{x}_k is independent of the measured output y_k . When configured in an open-loop manner, and given accurate initial conditions, the state-space model can predict future temperatures with root mean squared errors of 2.1%. In the case of precise initial conditions $\hat{x}_0 = x_0$ the estimates remain reasonably accurate with changes in inputs for all $k > 0$. In a real application, however, the precise initial temperatures of the system are not known since no absolute measurement of temperature

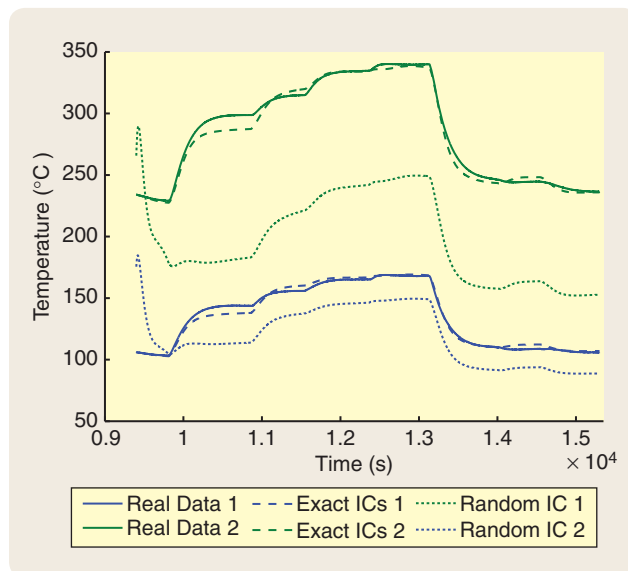


FIGURE 10 Evolution of the estimated state vectors for the state-space model with various initial conditions. Greater errors are observed for cases with inaccurate initial conditions. These inaccuracies are expected since no error feedback exists in this configuration, leaving estimates uncorrected.

is available. To simulate a situation with unknown initial conditions the model is tested with a random initialization of \hat{x}_0 to investigate the evolution of the state estimates over time. Larger errors are observed as expected for unknown initial conditions, with temperature predictions remaining inaccurate for the duration of the test. The two conditions are demonstrated in Figure 10, which shows the evolution of two system states as examples, representing two temperature measurements on the gas containment tube. Figure 11

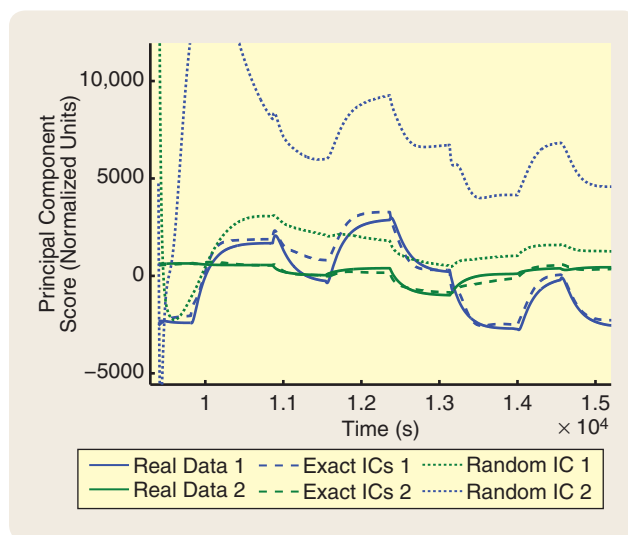


FIGURE 11 Evolution of the estimated outputs for the state-space model with various initial conditions. With inaccurate initial conditions, the output of the model does not follow the real output. Feedback is commonly used to compensate for this problem.

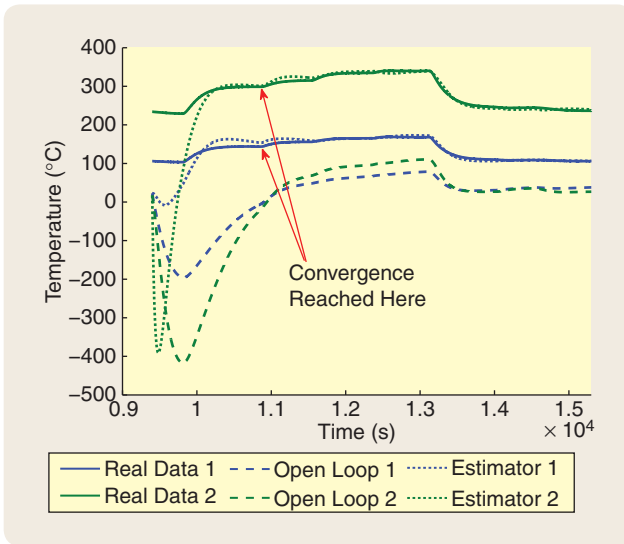


FIGURE 12 Comparison of state-prediction performance with and without error feedback. With error feedback in place, the state estimates converge to the true state values. This case illustrates a realistic condition, where initial conditions are unknown.

shows the open-loop behavior of the system outputs subjected to the same tests, depicting two of the three OES principal components on the same axis. As is the case with the state evolution, the output predictions are inaccurate with unknown initial conditions.

Closed-Loop Estimation

To accurately correct the state estimates when the initial states of the system are unknown, feedback of the measured system outputs is introduced. Equation (10) is used to update the state estimate \hat{x}_k in response to

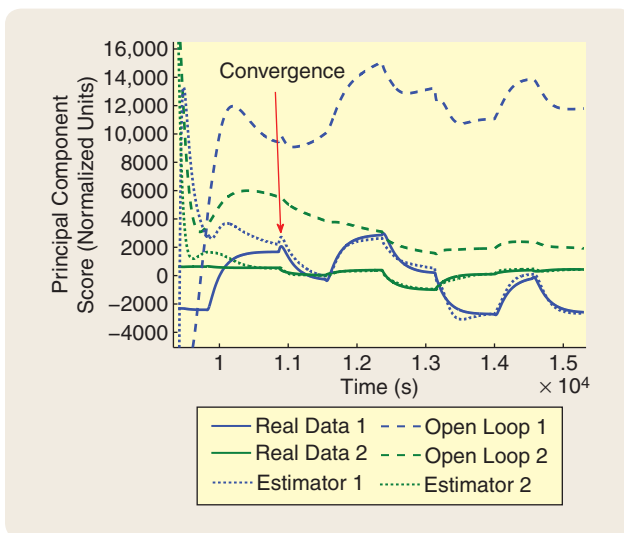


FIGURE 13 Comparison of the output prediction performance with and without error feedback. Output predictions converge to the true outputs when output feedback is in operation. In contrast, the open-loop estimation scheme produces inaccurate predictions.

the system output prediction error. Figure 12 shows the evolution of the predicted state vector with the model configured in closed-loop estimator form. A random initial condition is used to illustrate the scenario where the temperature is unknown at estimator startup. The open-loop performance is also shown on Figure 12 for comparison. Figure 13 shows the corresponding output behavior of the system for this configuration. It can be seen that both the estimated outputs and the estimated states, although starting with unknown initial conditions, converge toward the true values over time as a result of the error feedback implementation. The provision of feedback correction removes the open-loop requirement of exact initial conditions for estimator accuracy and gives root mean squared errors of $\sim 2\%$ after the estimator converges.

CONCLUSIONS

The VASIMR propulsion system is an ion propulsion system for spacecraft that uses magnetic fields to accelerate plasma to produce thrust. Undesired heat produced in the helicon section of VASIMR must be monitored and removed safely to avoid damage to system components, especially when higher power operating regimes are explored. This article demonstrates a strategy for distributed temperature estimation, based on OES measurement, and a model where the states represent the distributed temperature profile. OES provides a noninvasive measurement technique, which can be used as an output “correction” term for a state-estimation scheme.

In this application, it is shown that the 2048 OES channels recorded can be accurately represented by only three principal components for temperature estimation.

Use of the principal components as corrector terms in the state-space model dramatically improve model accuracy and the capability of the model to recover from unknown initial conditions and multiple system input changes.

ACKNOWLEDGMENTS

This research was performed at the Ad Astra Rocket Company Costa Rica laboratory in Liberia, Costa Rica. The authors would like to thank the staff of Ad Astra for their help and cooperation. This project was funded by FÁS Ireland and the Irish Research Council for Science Engineering and Technology (IRCSET).

AUTHOR INFORMATION

Shane A. Lynn (shane.a.lynn@eeng.nuim.ie) received the B.Eng. degree in computer engineering from the National University of Ireland, Maynooth, in 2006. He is currently pursuing a Ph.D. degree in engineering. His main research area is the state estimation of a plasma etch process used in semiconductor manufacture. He can be contacted at the Department of Electronic Engineering, National University of Ireland, Maynooth, Co. Kildare, Ireland.

John V. Ringwood received the Hons. Diploma in electrical engineering from Dublin Institute of Technology and the Ph.D. in control systems from Strathclyde University, Scotland, in 1981 and 1985, respectively. He is currently a professor of electronic engineering at the National University of Ireland (NUI), Maynooth, and associate dean of the Faculty of Engineering within the Faculty of Science and Engineering. He was the founding head of the Electronic Engineering Department at NUI Maynooth, serving as head from 2000 until 2005. His research interests include time series modeling, control of wave energy systems, control of plasma processes, and biomedical engineering. He is a chartered engineer, a fellow of Engineers Ireland, and a Senior Member of the IEEE.

Juan Ignacio Del Valle Gamboa obtained the B.Sc. degree in mechanical engineering from the University of Costa Rica and the M.Sc. degree in the same field from Delft University of Technology, in the Netherlands. He works as a thermal design engineer for Ad Astra Rocket Company Costa Rica, at the company's research lab in Liberia, Costa Rica.

REFERENCES

- [1] F. F. Chen, "Plasma ionization by helicon waves," *Plasma Phys. Control. Fusion*, vol. 33, no. 4, pp. 339–364, 1991.
- [2] E. A. Bering, III, and M. Brukardt, "Ion acceleration by single pass ion cyclotron heating in the VASIMR engine," in *Proc. 29th Int. Electric Propulsion Conf. (IEPC-2005-093)*, Princeton Univ., NJ, Oct. 2005.
- [3] T. W. Glover, F. R. Chang-Diaz, J. P. Squire, V. P. Jacobson, D. G. Chavers, and M. D. Carter, "Principal VASIMR results and present objectives," in *Proc. Space Technology and Applications Int. Forum*, Albuquerque, New Mexico, Feb. 2005, pp. 976–982.
- [4] J. P. Squire, F. R. Chang-Diaz, T. W. Glover, M. D. Carter, L. D. Cassady, W. J. Chancery, V. T. Jacobson, G. E. McCaskill, C. S. Olsen, E. A. Bering, M. S. Brukardt, and B. W. Longmier, "VASIMR performance measurements at powers exceeding 50-kW and lunar robotic mission applications," in *Proc. Int. Interdisciplinary Symp. Gaseous and Liquid Plasmas [CD-ROM]*, Akiu/Sendai, Japan, Sept. 2008.
- [5] NASA. (2003, June). *Mars Exploration Rover Launches*. Press kit [Online]. Available: www.jpl.nasa.gov/news/press_kits/merlaunch.pdf
- [6] S. Upson, "Rockets for the red planet," *IEEE Spectr. Mag.*, vol. 46, pp. 38–43, June 2009.
- [7] F. F. Chen and J. P. Chang, *Lecture Notes on Principles of Plasma Processing*. Norwell, MA: Kluwer, 2003.
- [8] R. W. Boswell and F. F. Chen, "Helicons—The early years," *IEEE Trans. Plasma Sci.*, vol. 25, no. 6, pp. 1229–1244, 1997.
- [9] R. W. Boswell and F. F. Chen, "Helicons—The past decade," *IEEE Trans. Plasma Sci.*, vol. 25, no. 6, pp. 1245–1257, 1997.
- [10] J. P. Rayner and A. D. Cheetham, "Helicon modes in a cylindrical plasma source," *Plasma Sources Sci. Technol.*, vol. 8, no. 1, pp. 79–87, 1999.
- [11] A. R. Ellingboe and R. W. Boswell, "Capacitive, inductive and helicon-wave modes of operation of a helicon plasma source," *Phys. Plasmas*, vol. 3, no. 7, pp. 2797–2804, 1996.
- [12] H. H. Yue, S. J. Qin, J. Wiseman, and A. Toprac, "Plasma etching end-point detection using multiple wavelengths for small open-area wafers," *J. Vacuum Sci. Technol. A.*, vol. 19, no. 1, pp. 66–75, 2001.
- [13] Z. Zhang, E. B. Martin, and A. J. Morris, "Fault-detection and diagnosis using multivariate statistical techniques," *Chem. Eng. Res. Design*, vol. 74, no. 1, pp. 89–96, 1996.
- [14] A. Afifi, V. A. Clak, and S. May, *Computer Aided Multivariate Analysis*, 4th ed. London, U.K.: Chapman & Hall, 2004.
- [15] D. C. Montgomery, G. C. Runger, and N. F. Hubele, *Engineering Statistics*, 2nd ed. New York: Wiley, 2001.
- [16] G. F. Franklin, J. D. Powell, and A. Emami-Naeini, *Feedback Control of Dynamic Systems*, 3rd ed. Reading, MA: Addison-Wesley, 1993.
- [17] D. Luenberger, "An introduction to observers," *IEEE Trans. Automat. Control*, vol. 16, no. 6, pp. 596–602, 1971.



» 25 YEARS AGO (continued from page 14)

fire control techniques at the beginning of this century [6]. This review was made necessary by the increasing range of naval guns. The outcome of the review was an increased interest in (i) the development of the gyro-compass—in iron ships, and with the increasing use of electricity in ships, great difficulty was experienced in using the magnetic compass—and (ii) in the stabilization of either the ship or the gun platforms and gun directors. Consideration was given to the possible improvement in accuracy through the reduction or elimination of yaw: "...my first approach to the problem of automatic steering in

order to eliminate yaw was therefore made more in connection with gunnery than with navigation" recalled Sir James Henderson in 1934 [7], who was against automatic steering, and this attitude did not change until the successful introduction of the commercial autopilot [8]. So although the tests carried out by Minorsky on the *New Mexico* were successful, the automatic steering was removed and further work discontinued.

REFERENCES

- [1] J. G. Ziegler, unpublished notes.
- [2] O. Mayr, *Feedback Mechanisms in the Historical Collections of the National Museum of History and Technology*. Washington, DC: Smithsonian Press, 1971, pp. 125–126.
- [3] S. Bennett, *A History of Control Engineering 1800-1830*. Peter Peregrinus, 1979, ch. 2.
- [4] Many papers on process control were published in *Trans. ASME* during the late 1930s and early 1940s, and a book summarizing some of the work was prepared by Ed. S. Smith, *Automatic Control Engineering*, New York: McGraw-Hill, 1944.
- [5] N. Minorsky, "Directional stability of automatically steered bodies," *J. Amer. Soc. Naval Eng.*, vol. 34, pp. 280–309, 1922.
- [6] P. Padfield, *Guns at Sea*. New York: St. Martin's Press, 1974; J. T. Sumida, "British capital ship design and fire control," *J. Mod. Hist.*, vol. 51, no. 2, 1979.
- [7] J. B. Henderson, "The automatic control of the steering of ships and suggestions for its improvement," *Trans. Inst. Naval Arch.*, pp. 20–31, 1934.
- [8] H. S. Howard, discussion of paper by Henderson, op. cit., p. 30.

